Electronic Supplementary Information (ESI) for:

Ion Type and Valency Differentially Drive Vimentin Tetramers into Intermediate Filaments or Higher Order Assemblies

Manuela Denz,[a] Manuel Marschall,[b] Harald Herrmann,[c] and Sarah Köster[a,d]

1 Influence of different buffers on the assembly of vimentin

Tris(hydroxymethyl)aminomethane (TRIS) and phosphate buffer (PB) are established buffer systems for *in vitro* vimentin assembly studies.[1–4] However, PB forms complexes with Ca^{2+}[5] and TRIS forms complexes with Co^{2+} and Zn^{2+}[6]. To overcome this difficulty, we introduce a more versatile buffer system in which we conduct a systematic study on the influence of different ions on vimentin assembly. To this aim, we compare the overall structure of the resulting filaments in PB, TRIS and 3-(N-morpholino)propanesulfonic acid (MOPS) using atomic force microscopy (AFM), and the radius of gyration of the cross-section, R_c, as well as the forward scattering, $I(0)$, using small angle X-ray scattering (SAXS). Measurements are performed at low (2 mM) and high (20 mM) buffer concentration, and the nonassembled (no additional salt) as well as the filamentous state (100 mM KCl added) of vimentin are investigated. These concentrations are chosen, as vimentin experiments in PB are usually carried out at low buffer concentrations. For TRIS the buffer concentration is typically increased from a low to a high concentration when assembly of the filament is initiated. In low ionic strength buffers, vimentin is in the tetrameric state as shown by analytical ultracentrifugation.[1] Accordingly, no filaments or aggregates are detected by AFM for the low buffer concentration, regardless of the buffer system used. The addition of 100 mM KCl triggers the assembly reaction and in all three buffer conditions long filaments are formed (Fig. S1 a-c). By contrast, at the high buffer concentration of 20 mM vimentin tetramers laterally associate into ULF-type structures as previously shown by electron microscopy. Upon the addition of 100 mM KCl, these ULF-type structures assemble into well-ordered filaments (Fig. S1 d-f). Thus, depending on the ionic strength, tetramers associate laterally into functional ULFs. Notably, these ULFs longitudinally associate to form extended filaments once the ionic strength is further increased by addition of 100 mM KCl.

To complement the AFM data, vimentin at low and high salt is investigated by SAXS. Again, the six different conditions are investigated and the scattering profiles are shown in Fig. S2a, b. For vimentin at low salt, the scattering profiles at 2 mM buffer concentration are very similar (darker symbols in Fig. S2a), whereas at the higher buffer concentrations (lighter symbols) the scattering profiles (i) behave differently form each other, (ii) all have a higher intensity at small q-values and (iii) are slightly steeper, indicating that the scatterers have a larger radius. The scattering profiles of vimentin filaments assembled in the presence of 100 mM KCl are similar for all six conditions (buffer type and concentration, see Fig. S2b).

Performing a Guinier analysis of the SAXS data, we retrieve the radius of gyration of the

[a] *University of Göttingen, Institute for X-Ray Physics, Friedrich-Hund-Platz 1, 37077 Göttingen, Germany; E-mail: sarah.koester@phys.uni-goettingen.de*
[b] *Physikalisch-Technische Bundesanstalt, Abbestraße 2-12, 10587 Berlin, Germany*
[c] *Institute of Neuropathology, University Hospital Erlangen, Schwabachanlage 6, 91054 Erlangen, Germany*
[d] *Cluster of Excellence "Multiscale Bioimaging: from Molecular Machines to Networks of Excitable Cells" (MBExC), University of Göttingen, Germany*

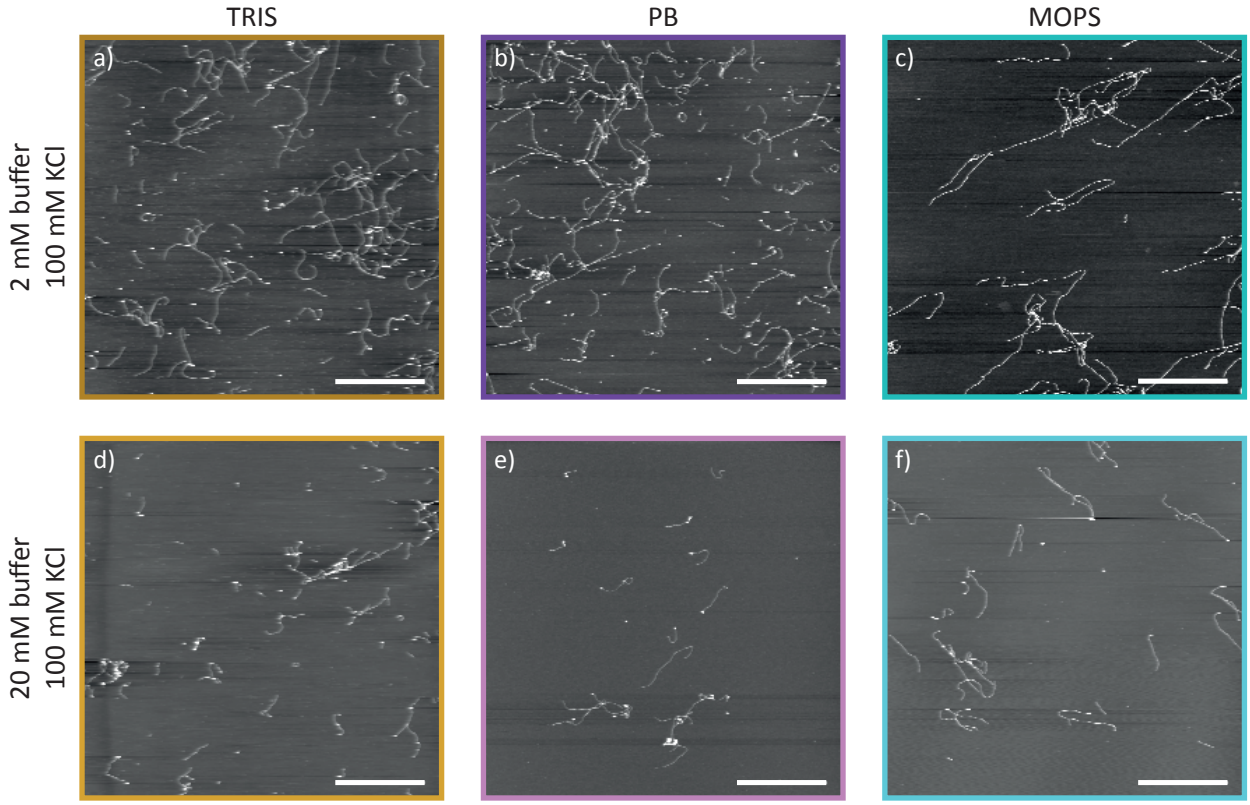

Figure S1 AFM images of vimentin structures at 2 mM and 20 mM in the three buffer systems, (left to right) TRIS, PB and MOPS. (a-c) Vimentin filaments assembled in the presence of 100 mM KCl at 2 mM buffer concentration. (g-i) Vimentin filaments assembled in the presence of 100 mM KCl at 20 mM buffer concentration. Scale bars: 5 μm.

cross-section R_c as well as the forward scattering $I(0)$. The data are shown in Fig. S2c and d, respectively. At 2 mM buffer concentration (darker symbols), the radius of gyration of the cross-section R_c as well as the forward scattering $I(0)$ agree between all buffers for the tetrameric as well as for the filamentous state, showing that vimentin behaves similarly in all three buffers, as long as the buffer concentration is kept low. The R_c values we retrieve for low salt (circles in Fig. S2c, left hand side) are similar to what was reported previously for the radius of vimentin tetramers.[7,8] R_c values obtained upon assembly (triangles in Fig. S2c, left hand side) agree with our expectation for vimentin filaments, *i.e.* a diameter of about 10-12 nm. Upon addition of 100 mM KCl, we also observe an increase in $I(0)$ (triangles in Fig. S2d, left hand side). This increase indicates that the number of monomers per cross-section increases.

At high buffer concentration, we find increased R_c values for the non assembled state, similar to the radii found for assembled vimentin at low buffer concentrations (circles in Fig. S2c, right hand side). This indicates ULF formation due to the high ionic strength of the buffers, see above. Interestingly, a difference between the radii for vimentin tetramers is found in the three different buffers at the high buffer concentrations, with the largest radius found for TRIS buffer and the smallest for MOPS buffer. Upon the addition of 100 mM KCl, R_c increases slightly, again with the largest radius found for vimentin filaments in TRIS and the smallest radius in MOPS buffer (triangles in Fig. S2c, right hand side). The $I(0)$ values for the non assembled state of vimentin in the high buffer concentration (circles in Fig. S2d, right hand side) are increased in the same manner as R_c, *i.e.* TRIS the most, MOPS the least, compared to the data taken at

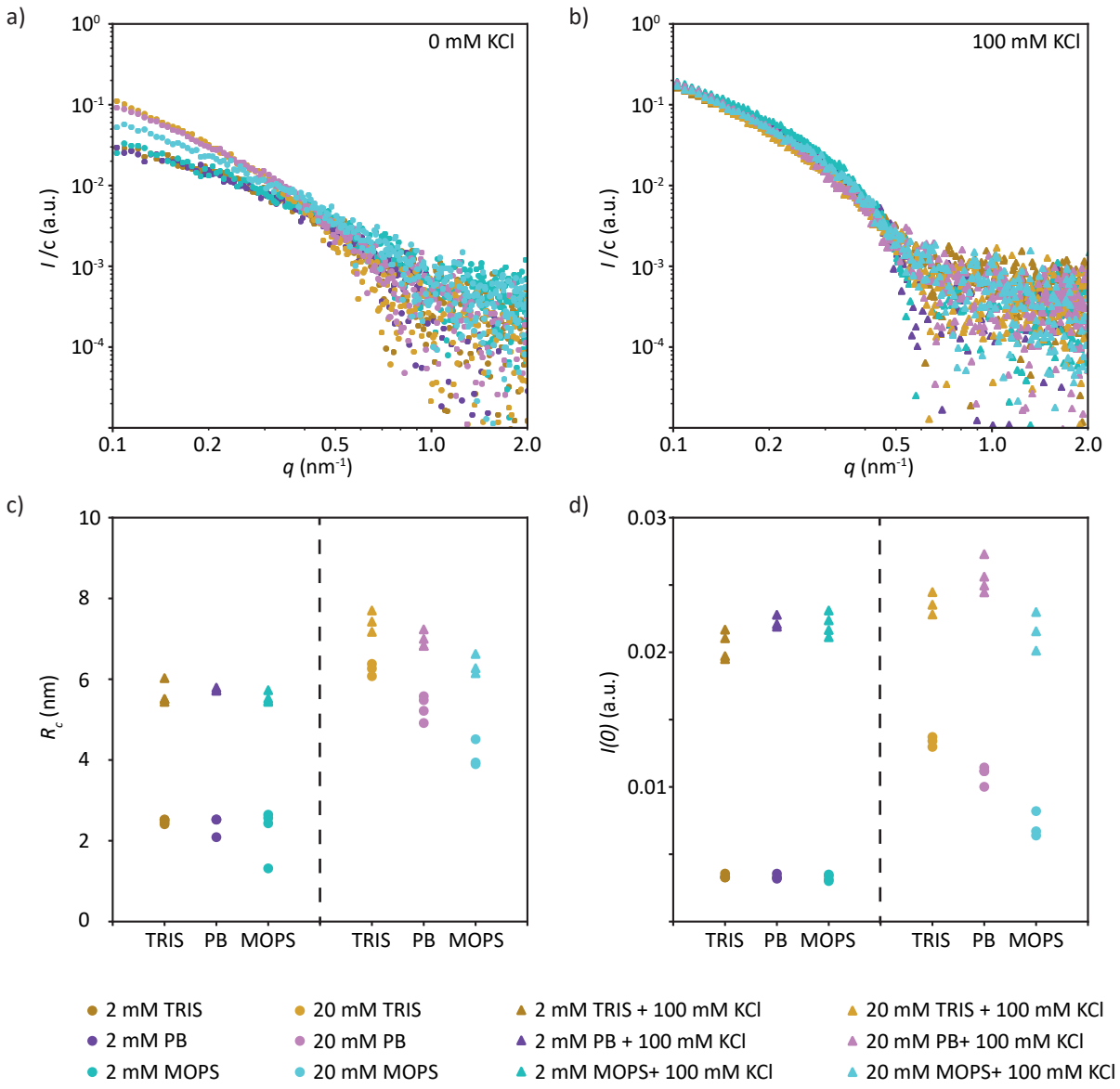

Figure S2 SAXS measurements of vimentin in three different buffer systems, TRIS, PB and MOPS, at 2 mM and 20 mM buffer concentration, without and with additional 100 mM KCl. (a) Scattering profiles for all three buffers (high/low buffer concentration) with no added KCl. (b) The scattering profiles for all three buffers (high/low buffer concentration) with 100 mM KCl added. (c) The radius of gyration of the cross-section, R_c, retrieved from Guinier analysis for all conditions. (d) The forward scattering, $I(0)$, for all conditions.

the low buffer concentration. Upon addition of 100 mM KCl, we also observe an increase in $I(0)$ (triangles in Fig. S2d right hand side). This increase is not in the same manner as for the the non assembled state at high buffer concentrations *i.e.* TRIS the most, MOPS the least. By contrast, when vimentin is assembled in PB it has the highest $I(0)$ value and when assembled in MOPS the lowest, indicating that vimentin filaments assembled in 20 mM PB are more densely packed than filaments in TRIS buffer (smaller R_c but larger $I(0)$). There is still a difference between the $I(0)$ values found for the filamentous state in the three different buffers, however it is not as pronounced as for the tetrameric state.

We show that there is no difference between vimentin in the three buffers at a buffer concentration of 2 mM and therefore establish MOPS as a versatile and suitable buffer system to

perform vimentin experiments with varying ions. Furthermore, we show that high buffer concentrations should be used with caution, especially when analyzing the tetrameric state of vimentin.

2 Azimuthal integration error for the scattering profiles

Fig. S3 shown an example of a scattering profile including the azimuthal integration error as error bars (vimentin assembled in the presence of 10 mM KCl). The error becomes notably larger at around $q = 1$ nm^{-1}, where the noise level is reached.

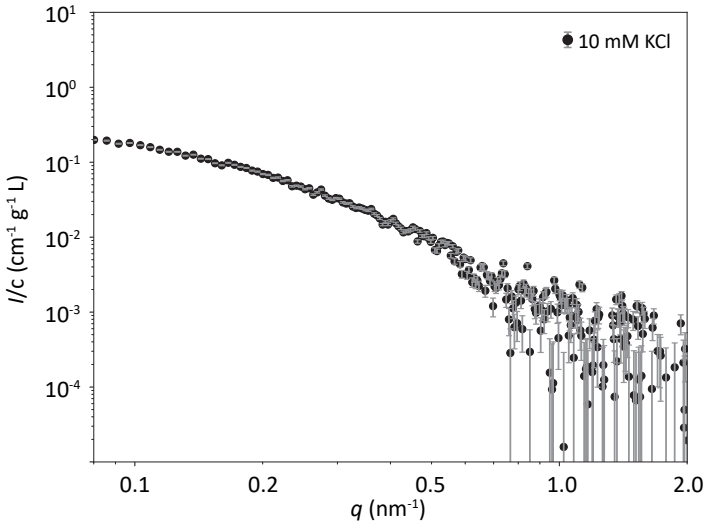

Figure S3 Scattering profile of vimentin assembled in the presence of 10 mM KCl. Error bars denote the azimuthal integration and are shown in gray.

3 Model Description

The model used to fit the $I(q)$ data of vimentin assembled in the presence of different ion types and concentrations is based on Ref. 2. Fig. S4a shows a schematic representation of a vimentin filament with the core in light blue and the tails protruding from the filament in dark blue. In Fig. S4b the electron density assumed for the model is shown which results in the filament scattering intensity

$$F_{\text{filament}}(q) = \beta[F_s(q) + \lambda b^2 F_c(q) + 2bS_{sc}(q) + b^2 S_{cc}(q)]. \tag{S1}$$

Here, β is the total scattering from the core per length, λ describes the average distance between the tails and b refers to the ratio between the scattering from the Gaussian cloud and the scattering from the core. The four terms in eqn. (S1) define correlation terms of the core and the chains. In particular,

$$F_s(q,R) = \left(\frac{2B_1(qR)}{qR}\right)^2 \frac{\pi}{q},$$

where B_1 is the Bessel Function of first kind and first order denotes the self correlation of the core. The self correlation of the chains is given by

$$F_c(q,R_g) = 2\frac{\exp(-(qR_g)^2) - 1 + (qR_g)^2}{(qR_g)^4}.$$

Modeling the cross correlation between the core and chains reads

$$S_{sc}(q,R,Rg) = \psi(q;R_g)\left(\frac{2B_1(qR)}{qR}B_0(qR)\right)\frac{\pi}{q}, \quad \text{with} \quad \psi(q;R_g) = \frac{1-\exp(-(qR_g)^2)}{(qR_g)^2}$$

where B_0 is the Bessel function of first kind and zero order. Finally, the cross-term between different chains is given by

$$S_{cc}(q;R_g) = \psi(q;R_g)^2 B_0(qR)^2\frac{\pi}{q}.$$

Using assumptions i) - iii) given in the main document and the additional incorporation of unassembled tetramers ($I_{\text{tetramer}}(q)$) yields a model description

$$F_{\text{tot}}(q) = aF_{\text{filament}}(q) + (1-a)I_{\text{tetramer}}(q) \tag{S2}$$

with five fit parameters, namely the relative scattering power of the tetramers a, the radius R, the radius of gyration of the chains R_g, b and β. For simplicity and in contrast to Ref. 2 we do not assume that the values for R follow a Gaussian distribution. We perform a global fit including all measured scattering curves per condition, see Figs. S6 to S8. A differential evolution solver[9], is employed to circumvent termination at local minima.

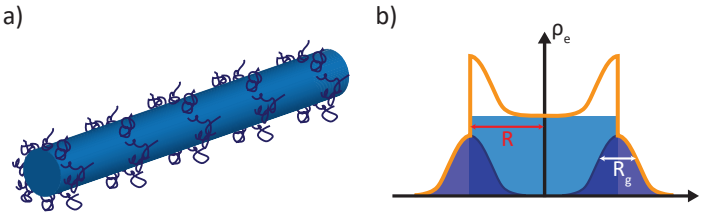

Figure S4 Model description. (a) Vimentin filaments can be modeled as cylinders with the tails (dark blue) of the monomers protruding from the filament core (light blue). (b) The radial electron density ρ_c of the model. In light blue the density of the cylinder is shown as a constant, yielding the radius R of the filament, whereas the tails are displayed in dark blue, providing information about the radius of gyration R_g of the tails. The orange line displays the total electron density with a semi-hollow core of the filament.

4 Precipitation Thresholds

For all multivalent ions, vimentin filaments precipitate when exceeding a certain threshold in ion concentration. This threshold is different for different ions. Fig. S5 shows the salt concentration range between the last non-precipitated and the first precipitated vimentin sample. With increasing valency of the ions, the precipitation threshold of vimentin decreases. For monovalent ions, above 300 mM ion concentration the protein solution turns opaque indicating that aggregates have formed. Consequently, SAXS measurements cannot be performed.

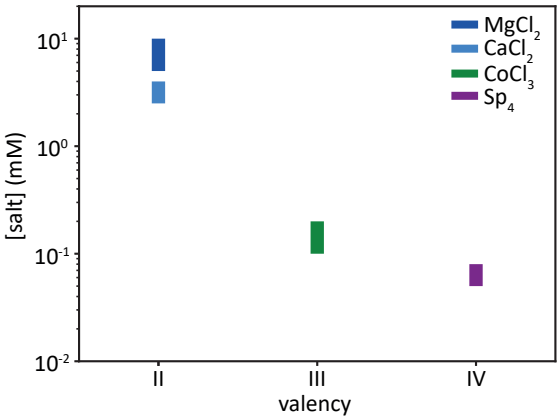

Figure S5 Ion concentration threshold for precipitation of vimentin assembled in the presence of different multivalent ions.

5 Individual Model Fits

In this section, the fits to the data from Fig. 3 of the main text are shown. Each ion concentration is displayed separately for a better overview. If more than one measurement was performed for one ion concentration all scattering profiles are shown. For determining the model fit, all scattering profiles obtained at the same condition are taken into account.

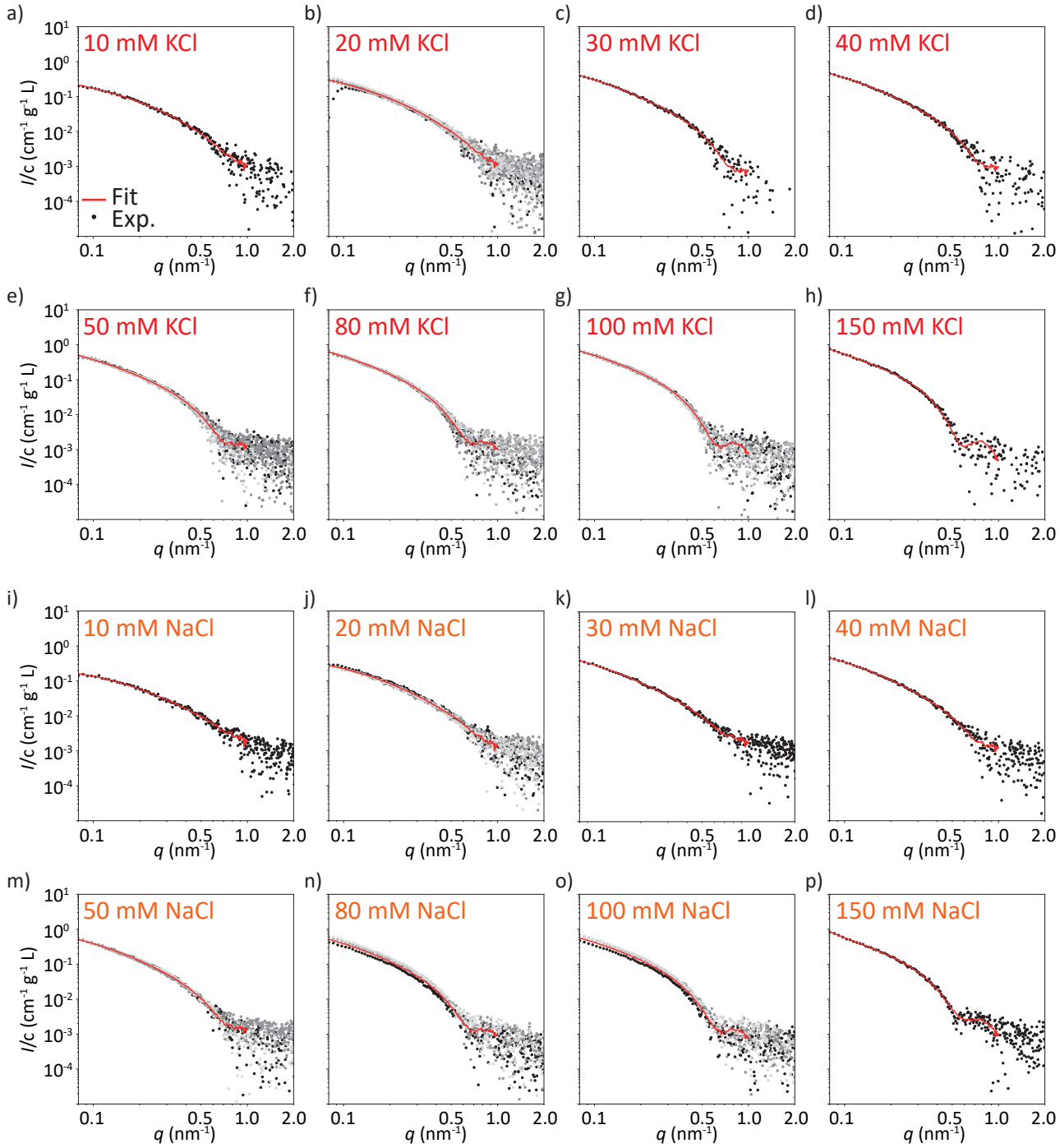

Figure S6 All individual scattering profiles and the corresponding model fits for (a-h) KCl and (i-o) NaCl. The red lines depict the fits, whereas the dots represent the experimental data.

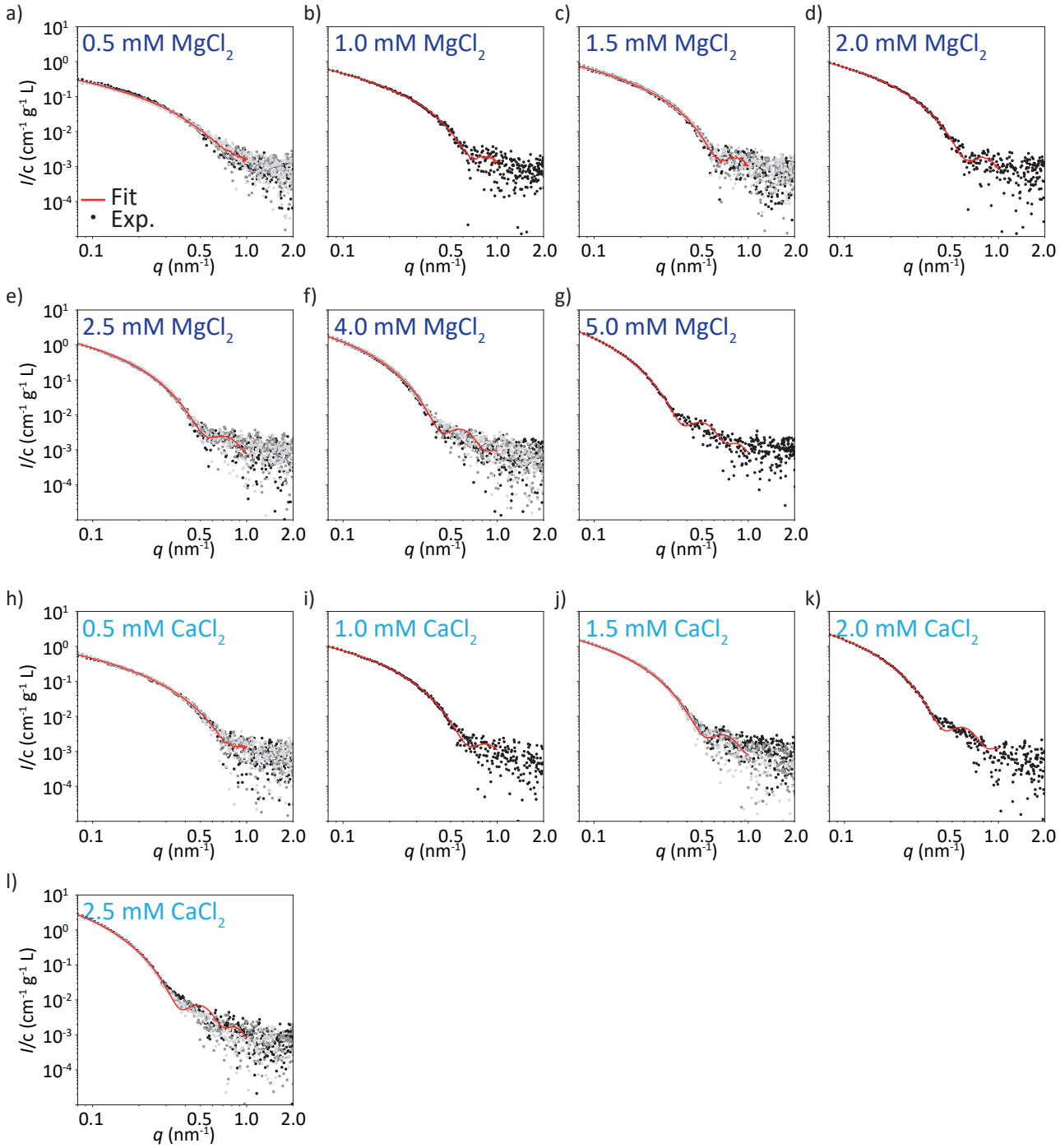

Figure S7 All individual scattering profiles and the corresponding model fits for (a-g) $MgCl_2$ and (h-l) $CaCl_2$. The red lines depict the fits, whereas the dots represent the experimental data.

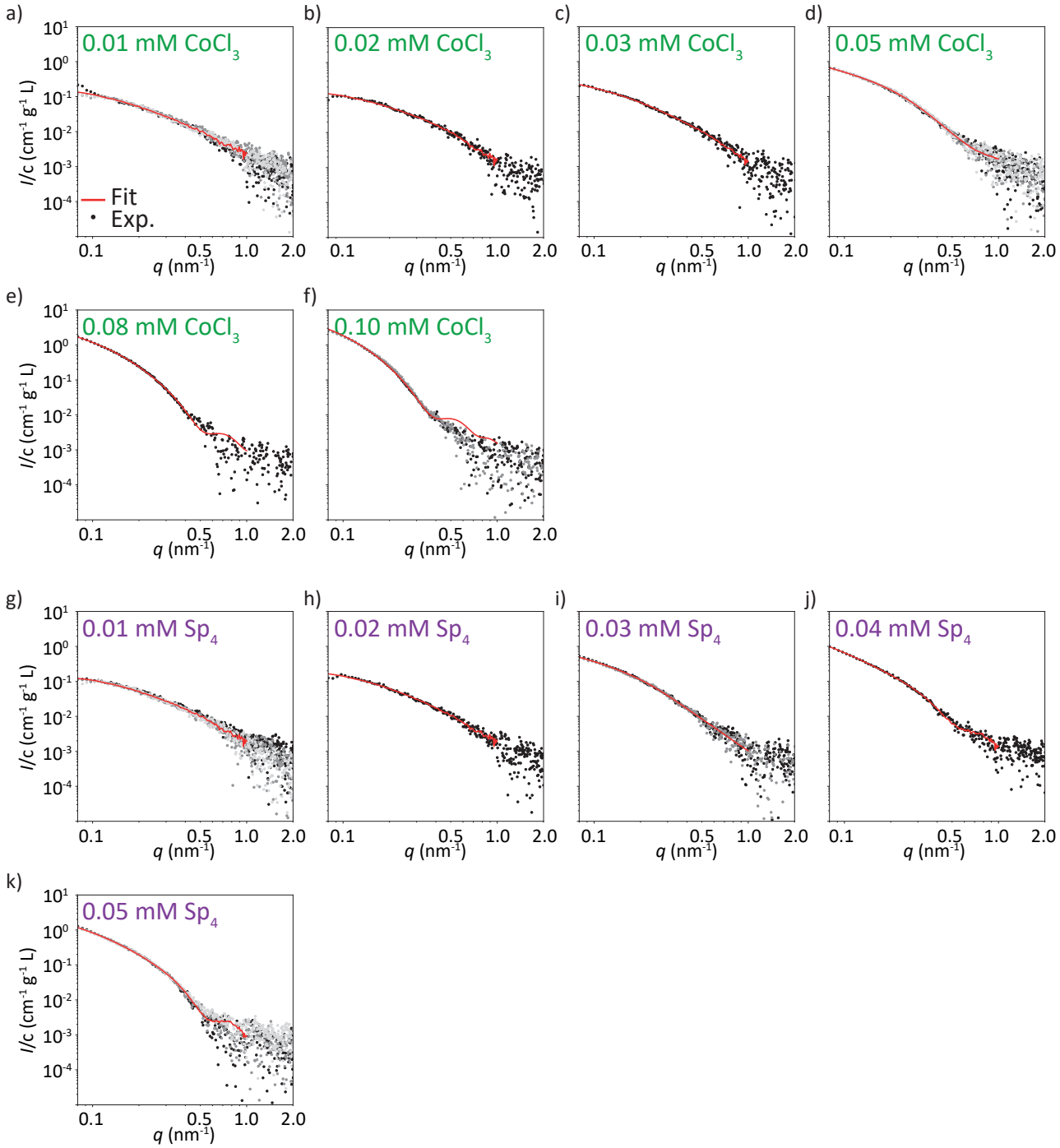

Figure S8 All individual scattering profiles and the corresponding model fits for (a-f) $CoCl_3$ and (g-k) Sp_4. The red lines depict the fits, whereas the dots represent the experimental data.

6 Correlation between $I(0)$ and the contribution of the tetramers to the scattering signal

The Guinier analysis provides the forward scattering $I(0)$ which is related to the number of subunits incorporated in the scatterers. $I(0)$ is dominated by the largest scatterers in the sample. From the model fit, we obtain the contribution of tetrameric scatterers, which are not incorporated in the filaments, to the overall scattering signal. Fig. S9 shows $I(0)$ plotted against contribution of the tetramers.

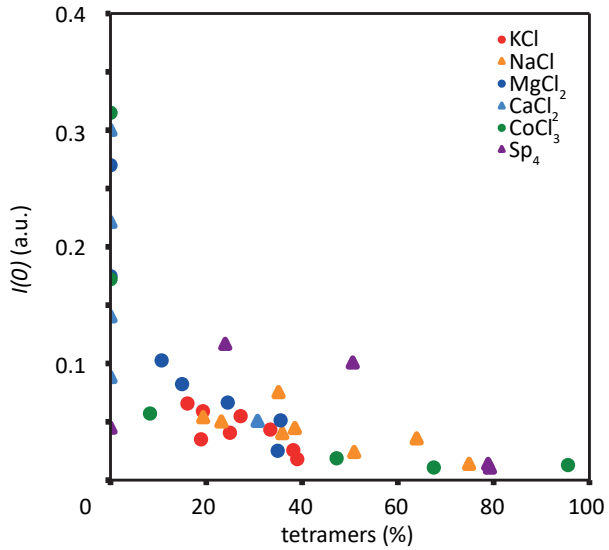

Figure S9 The forward scattering $I(0)$ retrieved from Guinier analysis against the fraction of tetramers derived from the model fit.

7 Radius of Gyration of the Tails

In addition to the radius of the filament and the relative scattering power of the tetramers, the model fit provides information about the radius of gyration (R_g) of the tails that protrude from the filament. Fig. S10 shows the radii of gyration retrieved for the six different ion types at their various concentrations. We observe that with increasing ion concentration, R_g increases as well.

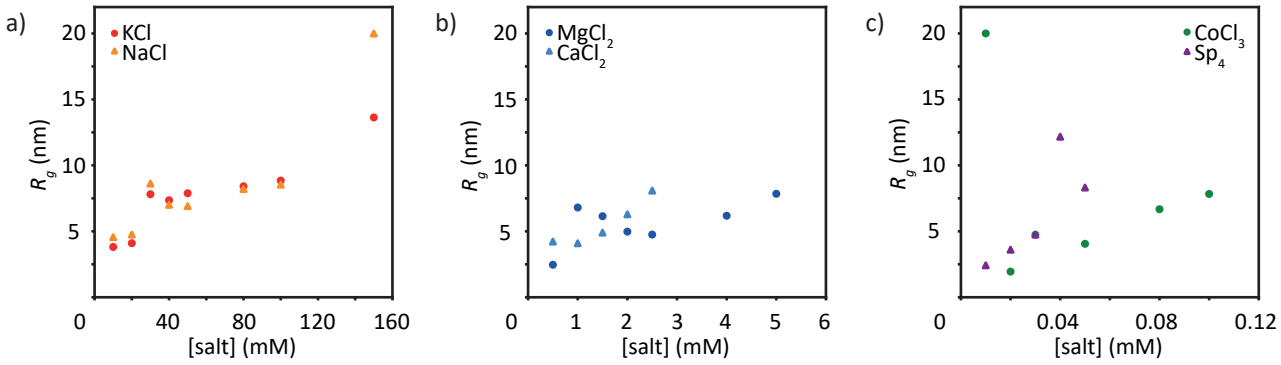

Figure S10 Radius of gyration R_g of the tails protruding from the filaments for a) monovalent ions, b) divalent ions and c) tri- and tetravalent ions.

References

1 N. Mücke, T. Wedig, A. Bürer, L. N. Marekov, P. M. Steinert, J. Langowski, U. Aebi and H. Herrmann, *J. Mol. Biol.*, 2004, **340**, 97–114.

2 M. E. Brennich, S. Bauch, U. Vainio, T. Wedig, H. Herrmann and S. Köster, *Soft Matter*, 2014, **10**, 2059–2068.

3 A. Premchandar, A. Kupniewska, K. Tarnowski, N. Mücke, M. Mauermann, M. Kaus-Drobek, A. Edelman, H. Herrmann and M. Dadlez, *J. Struct. Biol.*, 2015, **192**, 426–440.

4 J. Block, H. Witt, A. Candelli, E. J. Peterman, G. J. Wuite, A. Janshoff and S. Köster, *Phys. Rev. Lett.*, 2017, **118**, 048101.

5 M. C. Larson, M. R. Luthi, N. Hogg and C. A. Hillery, *Cytometry Part A*, 2012, **83A**, 242–250.

6 D. P. Hanlon, D. S. Watt and E. W. Westhead, *Anal. Biochem.*, 1966, **16**, 225–233.

7 H. Herrmann, M. Häner, M. Brettel, S. A. Müller, K. N. Goldie, B. Fedtke, A. Lustig, W. W. Franke and U. Aebi, *J. Mol. Biol.*, 1996, **264**, 933–953.

8 A. A. Chernyatina, S. Nicolet, U. Aebi, H. Herrmann and S. V. Strelkov, *Proc. Natl. Acad. Sci. U. S. A.*, 2012, **109**, 13620–13625.

9 R. Storn and K. Price, *J. Global Optim.*, 1997, **11**, 341–359.